Supporting information

Methods

Si bottom cell fabrication

Phosphorus-doped n-type Float Zone grown Si wafers with a thickness of 280 µm and resistivity of 2.0 Ω·cm were used for making efficient Si cell for tandem solar cell application. The double-side chemically polished Si wafer was RCA cleaned by using RCA 1 solution of NH_3: H_2O_2: H_2O = 1:1:7 and RCA 2 solution of HCl: H_2O_2: H_2O = 1:1:7.1% HF dip was done after both RCA1 and RCA2 cleaning. After standard RCA cleaning, Si wafers were oxidised in a tube furnace in O_2 at 1050 °C to grow a 20 nm layer of SiO_x as insulation for the non-active cell areas. Using photolithography, the SiO_x layer on the active cell area on the front surface and all of rear surface were etched using buffered hydrofluoric acid solutions. The active area of the Si and the tandem solar cells is defined to be 1 x 1 cm^2. Ultra-thin SiO_x was then grown chemically on both surfaces of the wafers through immersion in hot concentrated nitric acid for 30 minutes, followed by deposition of the intrinsic poly-Si layer using low-pressure chemical vapour deposition (LPCVD) using silane as the precursor. After deposition, the thickness of the poly-Si layers was measured to be approximately 80 nm using an ellipsometer and cross-sectional TEM measurement, both of which provide consistent results. It is worth noting that this thickness is much thinner than the poly-Si layers typically found in commercial TOPCon Si cells, where the poly-Si layer is generally over 100 nm. Further efforts are underway to reduce the thickness while simultaneously enhancing the passivation of both the n-type and p-type poly-Si layers. The Si substrate was then doped with boron[1] and phosphorus[2] substantially using standard industrial-relevant doping processes with a back-to-back method for separating the n and p sides. The sheet resistance of the poly-Si layers were measured to be between 200 to 220 Ω/□ based on the four-point probe test. Samples were annealed in forming gas (95% N_2, 5% H_2) at 425 °C for 30 mins. After removing the doped boron-glass and phosphorus-glass in a dilute hydrofluoric solution, a thermal ALD system is used for depositing TiO_2 films on both surfaces using the $TiCl_4$ precursor, with H_2O as the oxidant and N_2(g) as the purge gas. The chamber N_2(g) flow was set to be 200 standard cubic centimeters per minute (sccm). Each ALD cycle consisted of a 0.75 s pulse of $TiCl_4$ followed by a 0.050 s pulse of H_2O. Between each precursor pulse, a 0.75s purge under a constant flow (300 sccm) of research-grade N_2(g) was used. Finally, 500 nm of Al was deposited on the rear surface of the Si wafer using thermal evaporation to form rear contact. The wafers were subsequently laser-scribed to a size of 2 x 2 cm^2 before being utilized in the fabrication of tandem solar cells.

Perovskite cells fabrication

FTO/glass substrates for single-junction perovskite cells were sequentially cleaned with detergent for 90 min, followed by deionized (DI) water, acetone, isopropanol, ethyl alcohol and DI water for 15

minutes per step in an ultrasonic bath. FTO glass or Si bottom cells were then UV-ozone treated for 15 mins. The mesoporous TiO_2 layer was fabricated by spin-coating diluted TiO_2 paste solution (30NRD: Ethanol = 1:12 wt.) at 5000 rpm/5000 acc for 15 s, followed by annealing at 400 ^oC for 25 minutes. The PMMA: PCBM passivation layer was spin-coated at 4000 rpm/4000 acc for 15 s, then annealed at 100 ^oC for 10 mins. The PMMA: PCBM blend solution was prepared by dissolving 1 mg PMMA (Mw~120000, Sigma Aldrich) and 3 mg PCBM (Sigma Aldrich) into 1 mL Chlorobenzene. A layer of n-OACl was deposited on the substrate by spinning the n-OACl solution (2 mg/mL) at 5000 rpm/5000 acc for 15s, followed by annealing step at 100 ^oC for 10 mins. The perovskite solution contained 0.96 M PbI_2, 0.99 M FAI, 0.16 M $PbBr_2$, 0.18 M MABr, 0.13 M CsI, 0.065 M RbI, and 1.5 mol% $PbCl_2$ in 0.875 ml of anhydrous N,N′-dimethylformamide (DMF)/dimethyl sulfoxide (DMSO) (8:2, v/v). The multiple-cation perovskite precursor solution was deposited by spin coating at 2000rpm for 12 s using a ramp rate of 1000 rpm s^{-1}. The sample was then transferred to a vacuum jig and underwent a vacuum flashing process with 120 mTorr for 15 s and 1.5 Torr for 15s. The film was then heated on hot plate for 120 °C for 20 mins or 120 °C for 10 mins and then100 °C for 10 mins. A layer of n-BABr was deposited on the perovskite layer by dynamic spinning the n-BABr solution (1.15 mg/mL in Isopropanol) at 5000 rpm/1000 acc for 30s, followed by another annealing step at 100^oC for 10 mins. The hole transport layer of poly-TPD (EMNI, 200,000 K) were based on spinning coating solution (0.5 mg/mL in chlorobenzene) at 5000 rpm/5000 acc for 15s, followed by another annealing step at 100 ^oC for 5 mins. Then, Spiro-TTB (Lumtec.) was deposited on the samples by thermal evaporation at a rate of 0.1 A/s under a high vacuum of 8×10^{-7} torr. A 6.2 nm MoO_x layer was then deposited on the samples by thermal evaporation at a rate of 0.1 A/s. To complete the single-junction device, 100 nm full-area Au contacts were deposited on the sample using thermal evaporation through a shadow mask. The active area of the single-junction perovskite solar cell is defined to be 4 x 4 mm^2.

For the monolithic tandem device, the front transparent contact was fabricated by sputtering ~40 nm IZO on the MoOx buffer layer with 30 W of radio-frequency (RF) power under Ar plasma, with a chamber pressure of 1.5 mtorr for 60 min. The sheet resistance of the 40 nm IZO top layer is measured to be 120 Ω/□. The Au fingers and busbars were deposited using thermal evaporation through a shadow mask to complete the device. A textured foil made in house was applied on the front surface of the complete tandem device.[3] For the fabrication of anti-reflective foil, the liquid polydimethylsiloxane (PDMS) and a curing agent (Sylgard 184 Silicon Elastomer from Dow Corning) were mixed with 10:1 weight ratio. The mixture was applied onto the textured silicon wafer to replicate the pyramidal features onto the PDMS. The PDMS layers were then left in air at room temperature for 48h to solidify and dry.

Device encapsulations and the stability tests

The tandem solar cells are encapsulated with edge sealing method.[4] In detail, the tandem devices are enclosed between two 1mm Framed SuperWhite Glass panels, sealed at the edges using HelioSeal™ PVS 101 polyisobutylene (PIB) sealant in a nitrogen glove box. To establish electrical connections with the top and bottom electrodes of the tandem devices, external Tin/Lead wires were used, connected by tinned-plated copper strips and Ag paste. These connections extend beyond the cover glass to the exterior. The module, along with a custom-made metal jig, was then placed on a hot plate for a 20-minute thermal treatment at 95 °C to soften the PIB. Subsequently, the screws at the corners of the jig are tightened, applying pressure exceeding 20 KPa on the surface. The entire module is then allowed to cool down, releasing any inner stress, for a minimum of 24 hours.

For the light-dark cycle stability test, the encapsulated tandem solar cells are exposed to light-dark cycles in ambient containing 12 hours of 1-sun light illumination and 12 hours stored in dark under open-circuit condition. For the light-heat stability test, the encapsulated device is biased at 1V, a voltage close to V_{MPP}, under continuous 1-sun illumination at 55 ± 5 °C in ambient. The cells undergo *J-V* measurement at regular intervals. For the damp-heat test, the encapsulated device is placed inside an environmental chamber with at 85 °C and 85% RH and were taken out for *J-V* measurement at certain intervals.

Characterization Details

J-V Measurement

J-V measurements were taken on a solar simulator system (Wavelabs Inc.) under 1 sun-condition (AM 1.5G, 1000 W/m^2, 25 °C). A certified Fraunhofer CalLab reference cell was used to calibrate the light intensity prior to the measurements. For the cell efficiency measurement, the cells were tested in a custom-built measurement jig under a flow of N_2 gas. Unless otherwise stated, all the measurements taken at a scan rate of 50 mV/s with a voltage step of 0.01 V. We also emphasize that, for all stability measurements, the tandem cells are encapsulated to prevent degradation under external agents such as moisture and oxygen. Robust encapsulation is crucial for the viability of commercial solar modules, especially those based on perovskite cells.

External quantum efficiency (EQE) Measurement

EQE measurements were performed using a QEX10 spectral response system from PV measurements Inc. For perovskite/Si tandem solar cells, EQE spectra were measured without encapsulation in ambient (relative humidity around 40-65%) in the wavelength range from 300 to 1200 nm with a scanning step of 10 nm. Xenon arc lamp was used as the broadband light source (with a chopper frequency of around 80 Hz) fed into a double grating monochromator to produce monochromatic light. The perovskite top cell was measured while saturating the bottom cell with a red light bias at the

wavelength of 1050 nm and the Si bottom cell was measured by saturating the top cell with a blue light bias at the wavelength of 550 nm.

Material Characterization

The films' optical properties (transmittance, absorbance) were measured with a Perkin Elmer Lambda 1050 UV-vis-NIR spectrophotometer. For cross-sectional imaging, a Helios Nanolab 600 FIB system was used. Prior to the cross-sectional imaging, a ~ 2 μm protection layer of Pt was deposited on the substrate.

XRD characterization was conducted using a Bruker D2 phaser diffractometer operated at 30 kV, 10 mA at 2θ (Cu Kα) 10-80° with a step size of 2° and scan speed of 2.3°/min. The micro-photoluminescence (μPL) characterization was conducted on a self-developed μPL system. The sample was excited by a pulsed OPO laser at 532 nm. For steady-state spectral PL, the signal was detected by Glacier X TE Cooled CCD Spectrometer with a detection range of 200 nm to 1050 nm. For time-resolved PL (TRPL), the signal was detected by id110 VIS 100MHz Photon Detector operated in free-running mode.

For X-ray photoelectron spectroscopy (XPS) and UV light photoelectron spectroscopy (UPS) characterization, a SPECS (Berlin) machine was used. For XPS measurement, X-ray emission was conducted with Mg Kα line (12kV-200 W) anode from an UHV non-monochromatic source. High-resolution scans at a pass energy of 10 eV were recorded after a survey scan for characterizing the chemical states. The excitation energy was 1253.6 eV.

UPS was applied to determine the occupied electron states of a sample surface and the work function from secondary electron distribution. Electrons are emitted from the sample surface with a UV radiation of 21.22 eV excitation energy and collected by a detector.

High-Resolution Transmission Electron Microscopy (HR-TEM): For HR-TEM characterisation, the images were captured by JEOL JEM-F200 (E10) Multi-Purpose FEG-S/TEM system at -180°C. The specimen for TEM is prepared with Focused Ion Beam (FIB) by FEI Helios 600 NanoLab.

Atomic-force microscopy (AFM): The AFM images were detected by Nanosurf CoreAFM. The samples were scanned at the rate of 2s/line with a resolution of 256 points/line.

Drift-diffusion simulation details

Simulations were performed using COMSOL Multiphysics v6.1. Details of the model can be found in previous publications.[5, 6] Simulation parameters are tabulated below:

Table S1. Device parameters used in the simulation.

Parameter	Value [unit]
Hole Transport Layer	
Relative Permittivity	3
Band Gap	3 V
Electron Affinity	Variable, see text
Effective density of states, valence band	10^{20} cm^{-3}
Effective density of states, conduction band	10^{20} cm^{-3}
Electron mobility	0.01 cm^2/Vs
Hole mobility	0.01 cm^2/Vs
Dopant defect concentration (p-type)	10^{17} cm^{-3}
Thickness	50 nm
Electron Transport Layer	
Relative Permittivity	24
Band Gap	3.2
Electron Affinity	3.9 V
Effective density of states, valence band	10^{20} cm^{-3}
Effective density of states, conduction band	10^{20} cm^{-3}
Electron mobility	0.1 cm^2/Vs
Hole mobility	0.01 cm^2/Vs
Dopant defect concentration (n-type)	10^{15} cm^{-3}
Thickness	50 nm
Perovskite Layer	
Relative Permittivity	64
Band Gap	1.68 V
Electron affinity	4 V
Effective density of states, valence band	10^{19} cm^{-3}
Effective density of states, conduction band	10^{19} cm^{-3}
Electron mobility	10 cm^2/Vs
Hole mobility	10 cm^2/Vs
Direct recombination coefficient	5.3 x 10^{-11} cm^3/s
Photocurrent density, when illuminated	20.2 mA/cm^2
Thickness	400 nm
Cation Concentration	10^{16} cm^{-3}
Anion Concentration	10^{16} cm^{-3}
Cation Diffusivity	10^{-8} cm^2/s
Anion Diffusivity	10^{-11} cm^2/s
Bulk midgap defect density	0, 5x10^{15} cm^{-3}
HTL Interface defect density	0, 10^7 cm^{-2}
TCO Layer	
Relative Permittivity	4
Band Gap	4 V
Electron affinity	4.3 V
Effective density of states, valence band	10^{19} cm^{-3}
Effective density of states, conduction band	10^{19} cm^{-3}
Electron mobility	5 cm^2/Vs
Hole mobility	1 cm^2/Vs
Thickness	130 nm
Dopant defect concentration (n-type)	10^{20} cm^{-3}

Techno-economic analysis details

In previous work, the cost of manufacturing the previous ANU tandem (ANU_Ref, reported in Shen's work[3]) was calculated.[7] In this work we estimate the cost of the new ANU tandem (ANU_Demo) described in this work. The key differences in processing between these two architectures are shown in Table S2.

Table S2 – Key process differences between ANU_Ref [3] and ANU_Demo reported in this work.

	ANU_Ref	**ANU_Demo**
Si cell	n-type wafer Diffuse top and bottom	n-type wafer SiO_2 + polysilicon Diffuse top and bottom
Si Rear contact	SiNx passivate rear SP Ag	ALD TiO_2 SP Al
Interface	HF Clean	None
ETL	ALD TiO_2 m-TiO_2 PMMA/PCBM	ALD TiO_2 m-TiO_2 PMMA/PCBM
Perovskite	CsRbFAMAPbIBr + CBZH Vacuum flash	CsRbFAMAPbIBr + CBZH Vacuum flash
HTM	Spin-coat Spiro-OMeTAD	Spin-coat Poly-TPD Evaporate Spiro-TTB
Buffer	MoOx	MoOx
Contact	Sputter front contact Ag evaporate	Sputter front contact Ag evaporate
AR	Textured foil	Textured foil

Compared to the Chang's work,[7] there are four new processes that require a cost estimate.

- Poly-silicon/SiO_2 passivating layers instead of diffused junctions with SiNx passivation.

Kafle *et al.* estimates the cost of a number of TOPCon process steps.[8] One process step that is very similar to the poly-silicon/SiO_2 contact is the LPCVD process that deposits an oxide and a-Si (i) at 0.27 US cents/Wp at 23.5% efficiency. For this work, we assume the same wafer size as Chang 2020 (244 cm^2), so at 23.5% efficiency, each wafer is 5.7 W. This means the LPCVD process is approx. 1.5 US c/wafer. Since this sequence requires this same layer on both sides of the silicon wafer, we assume a cost of 3.0 US c/wafer. Note that this is conservative, since there may be cost benefits from depositing on both sides simultaneously.

- ALD TiO_2 + Al screen printed rear of the Si cell instead of Ag/Al.

In Chang's work,[7] the cost of an ALD TiO_2 layer was estimated using a bottom-up cost model. In this work, this layer is present on both the front and rear sides of the Si wafer. We thus assume that the single-sided process previously assumed for the front side is carried out on both sides sequentially. Note that this is conservative, since there may be cost benefits from depositing on both sides simultaneously.

Note that the TiO_2 ALD cost estimate made in this work is based on different assumptions to that of [Chang et al.],[9] which also estimated the cost of ALD deposition of TiO_2. That other paper estimated the cost of depositing a 3nm TiO_2 layer with Tetrakis(dimethylamido)titanium (TDMAT) as the precursor, based on experimental data from UNSW researchers. The overall cost is approximately 20 times higher compared to the previous work on other cell structure.[9] We note that for presenting a conservative estimate of the cost, we opted to use a relatively thick TiO_2 layer in our cost study. In practice, a thinner TiO_2 layer, equivalent to half of the thickness employed in the technoeconomic study (54 nm), has proven to be effective in the current tandem design. Therefore, the overall cost of the ALD TiO_2 discussed here falls at the upper end of the estimation. Additionally, TiO_2 with similar hole-conducting properties has been demonstrated using a cost-effective and scalable sputtering process,[10, 11] presenting a promising opportunity for further cost reduction and enhance industry relevance.

In Chang's work,[7] the cost of the rear side metallisation of the Si cell (assumed screen printed Ag) was estimated at 60% of the cost of metallization of PERC cells. In this work, it was observed that evaporated Al was an effective contact at the rear of the Si cell, so in this work we assume that this can be achieved with a screen printed Al paste. The relative cost of screen-printing Al versus Ag paste is assumed in this work to be halved, although the actual reduction in cost may be greater, since Al is around 100 times lower cost than silver.

- Spin-coat Poly-TPD + Evaporate Spiro-TTB instead of spin-coating Spiro-OMeTAD/PTAA

The Poly-TPD concentration assumed is the optimum found in this work, 0.5 mg/mL. The usage estimate is 60 uL of solution for a 2 x 2 cm^2 glass, usage scaled with area (61 times larger area for 244 cm^2 compared to 4 cm^2). Usage is thus 3.66 mL/wafer. This means 1.83 mg Poly-TPD / wafer. (+/- 20% as assumed in Chang's work[7]). The cost of Poly-TPD is taken from Chang 2020 (1g costs 406.8 USD). The solvent was assumed to be Chlorobenzene.

Evaporation of Spiro-TTB, assumption is for 10nm thickness, and evaporation rate of 0.2 A/s. Using the same estimation process as Chang's work,[7] the total deposition time for this layer is 100A / 0.2 A/s = 500s. This would mean a throughput that is 1900 / 500 = 3.8 times faster than the reference Au evaporation process, which was assumed to have a 30 m^2/h throughput. The throughput for this process is thus assumed at 114 m^2/h (+/- 30%). For material usage, assuming a density of Sprio-TTB

of 0.8 g/cm^3.[12] we would expect 1m^2 of module, 10nm thick material to have 0.01 cm^3 of Spiro-TTB = 0.008 g/m^2. Since evaporation has some material wastage, we assume nominal material utilization of 40% (low utilization of 30%, high utilization of 70%). This gives a usage per m^2 of 0.02 (0.011 - 0.027) g/m^2. Assuming 36.6 wafer /m^2 can be deposited within the chamber, this means the usage per wafer is 0.000546 (0.000312 – 0.000729) mg/cell. The cost of Spiro TTB is assumed the same as Chang's work (5g costing).[7]

Supporting figures：

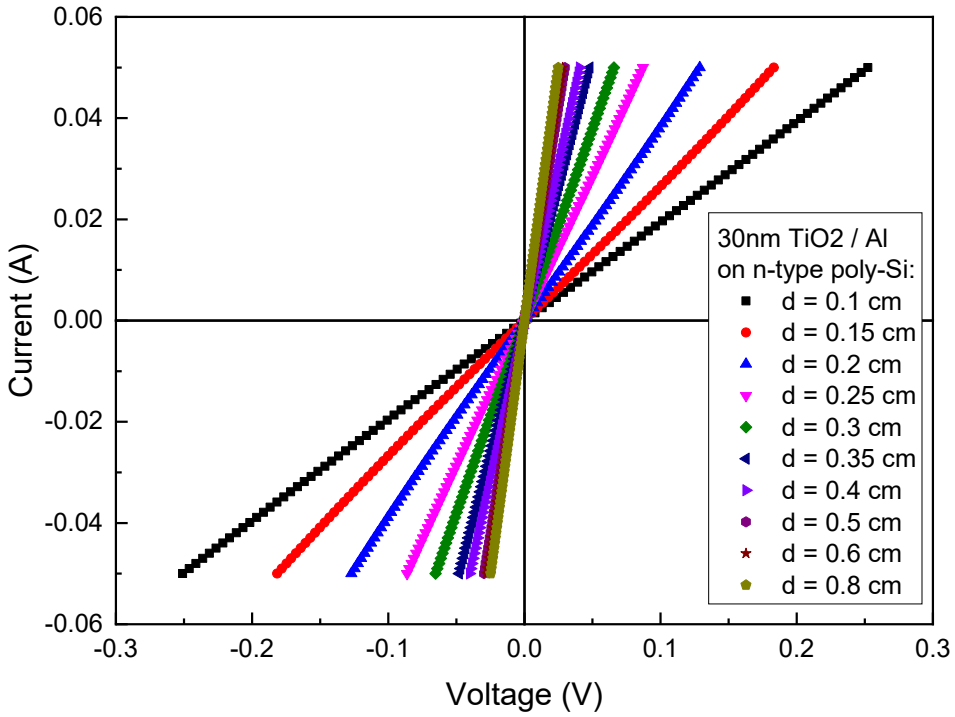

Fig S1. *I-V* curves of TiO_2/Al stack on n-type poly-Si layer using the Cox-and-Strack method.

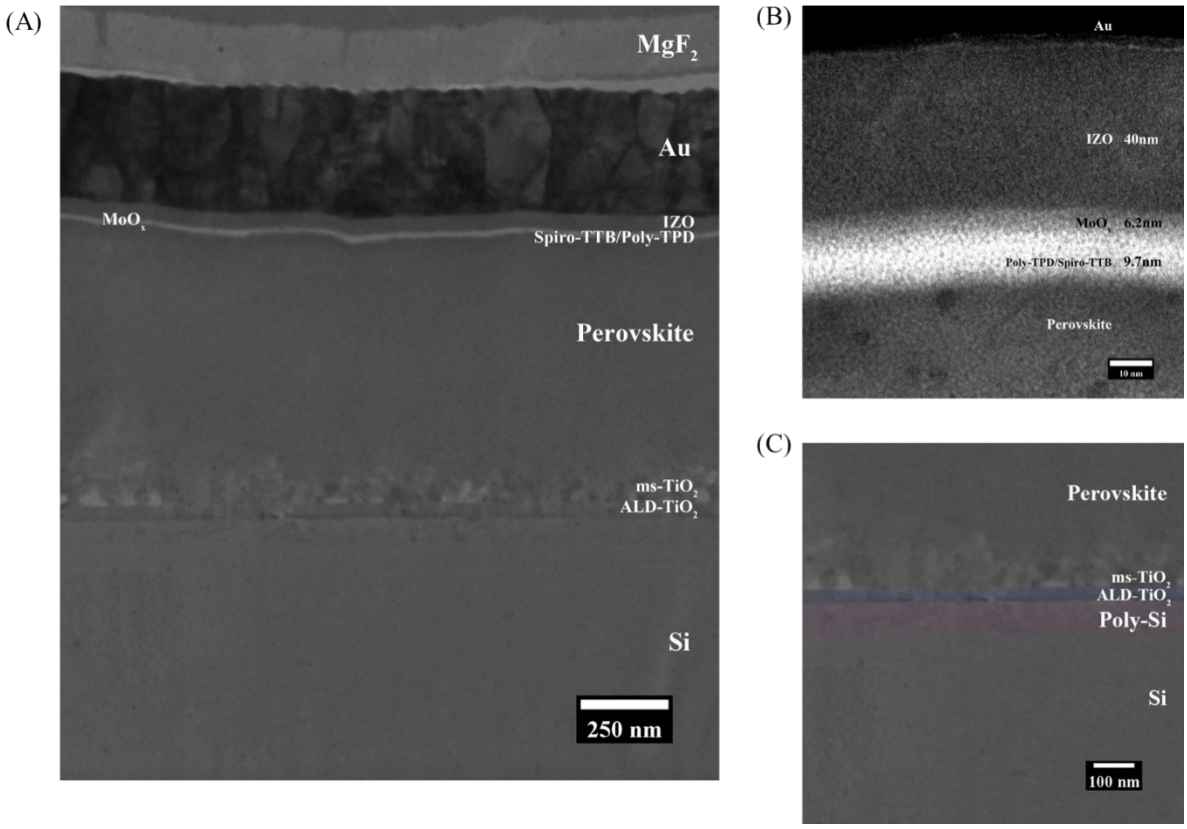

Fig S2. Cross-sectional High-resolution Transmission Electron Microscopy (HR-TEM) images of (A) the tandem solar cell; (B) the perovskite/Poly-TPD/Spiro-TTB/MoO_x/IZO/Au interface; (C) the interconnect between the p-type poly-Si/SiO_x passivation contact in the Si subcell and the ALD-TiO_2/ms-TiO_2/perovskite on the bottom side of the perovskite subcell in a tandem solar cell.

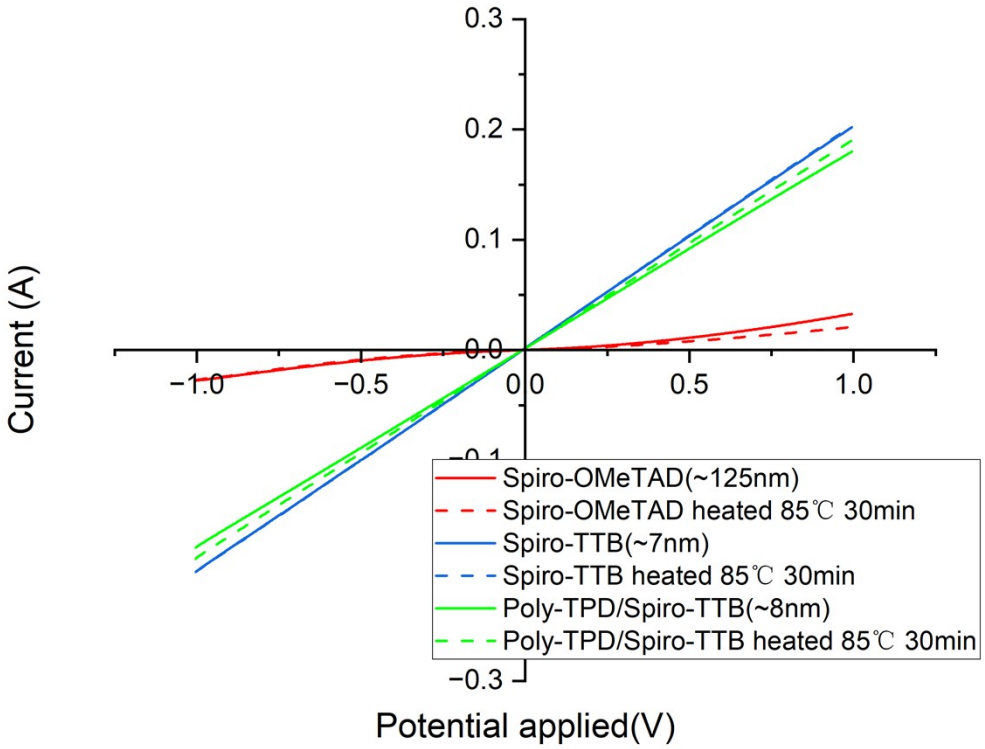

Fig S3. *I-V* characterization of different HTLs of Spiro-OMeTAD, Spiro-TTB, and Poly-TPD/Spiro-TTB bilayer before and after the thermal aging at 85 °C for 30 min. The test structure is based on Glass/FTO/HTL/Au, with the same dimension and layout used for the single-junction perovskite solar cells.

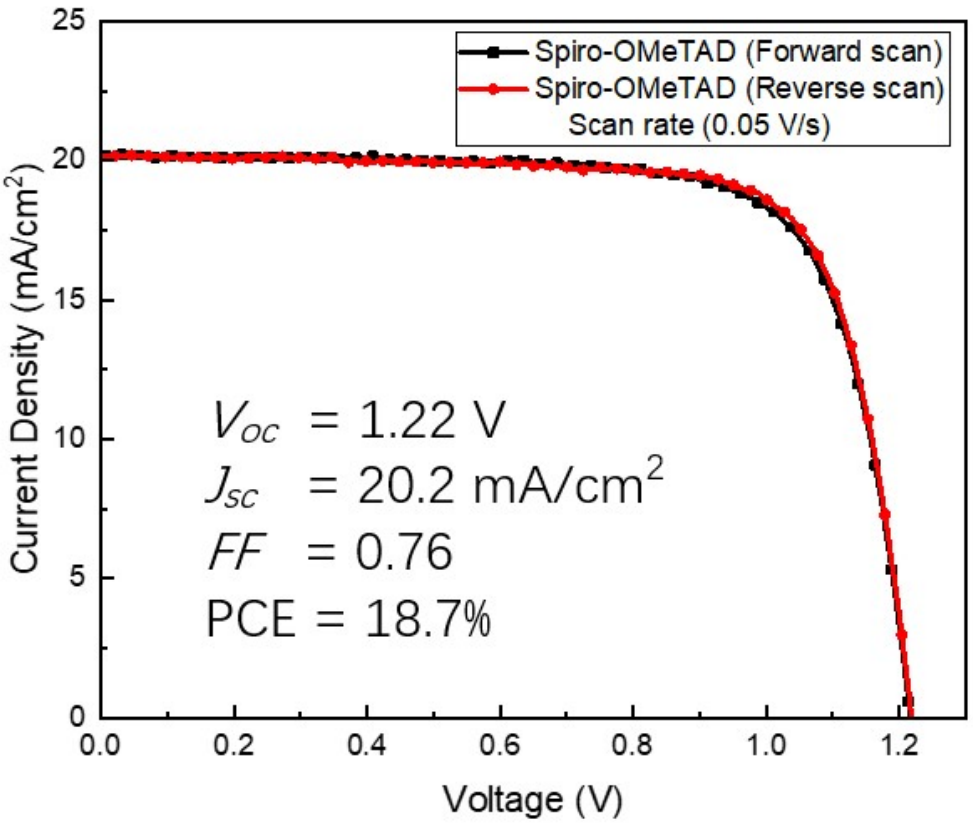

Fig S4. *J-V* curve of champion single-junction perovskite device based on Spiro-OMeTAD as HTL. The photovoltaic parameters are extracted from the *J-V* curve obtained with reverse scanning.

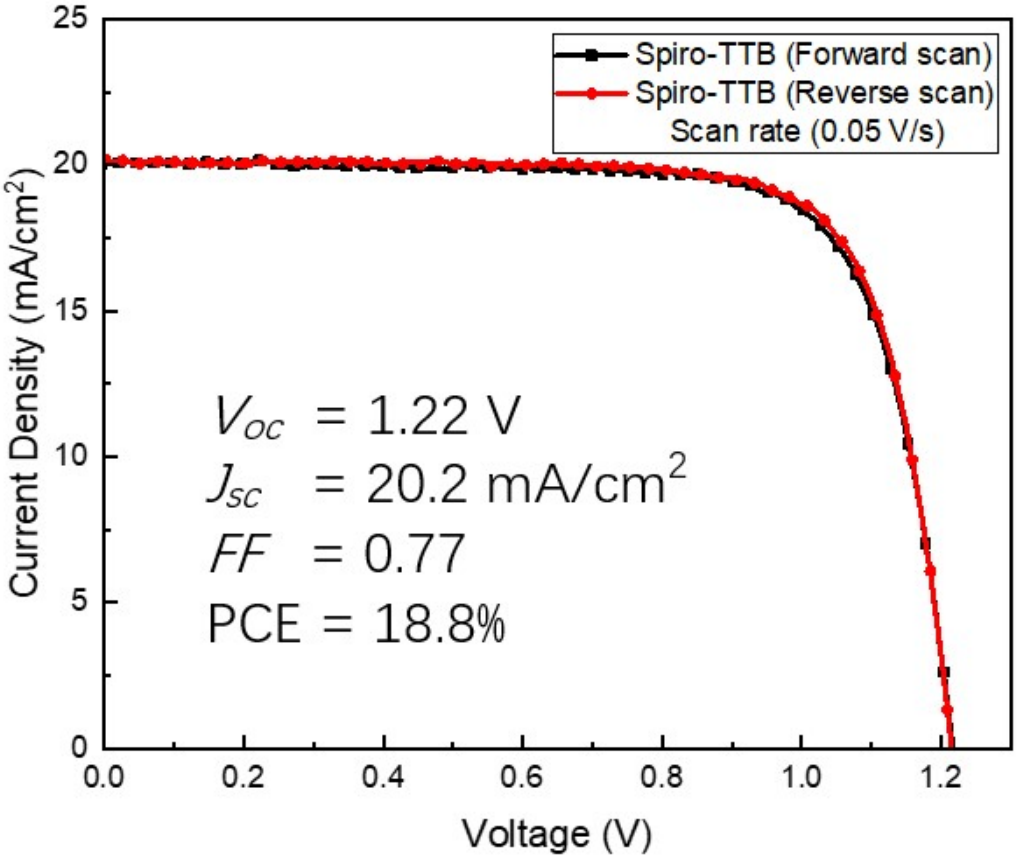

Fig S5. *J-V* curve of champion single-junction perovskite device based on Spiro-TTB as HTL. The photovoltaic parameters are extracted from the J-V curve obtained with reverse scanning.

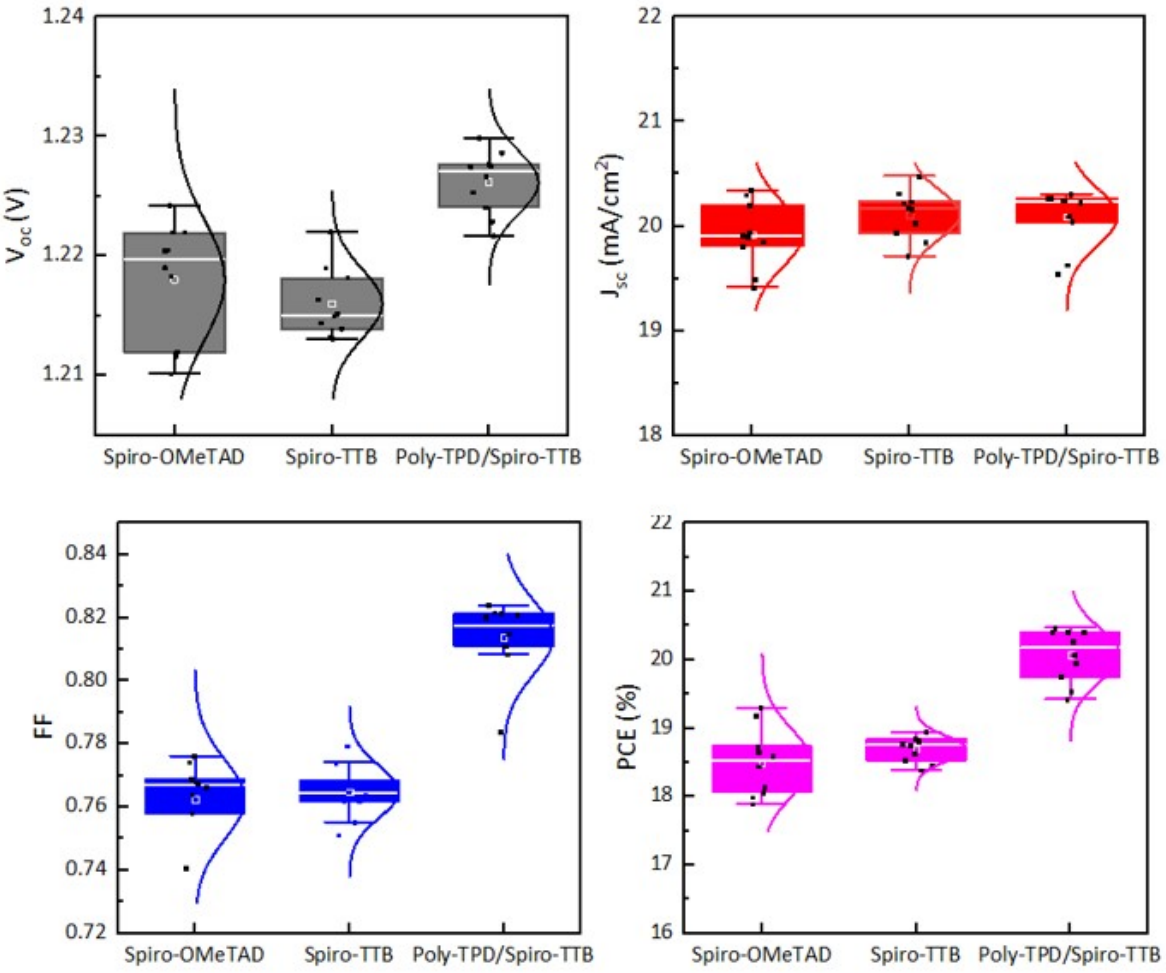

Fig S6. Statistical photovoltaic parameters of ten individual devices from three separate batches including V_{oc}, J_{sc}, FF and PCE of single-junction perovskite solar cells with different HTLs including Spiro-OMeTAD, Spiro-TTB and Poly-TPD/Spiro-TTB bilayer.

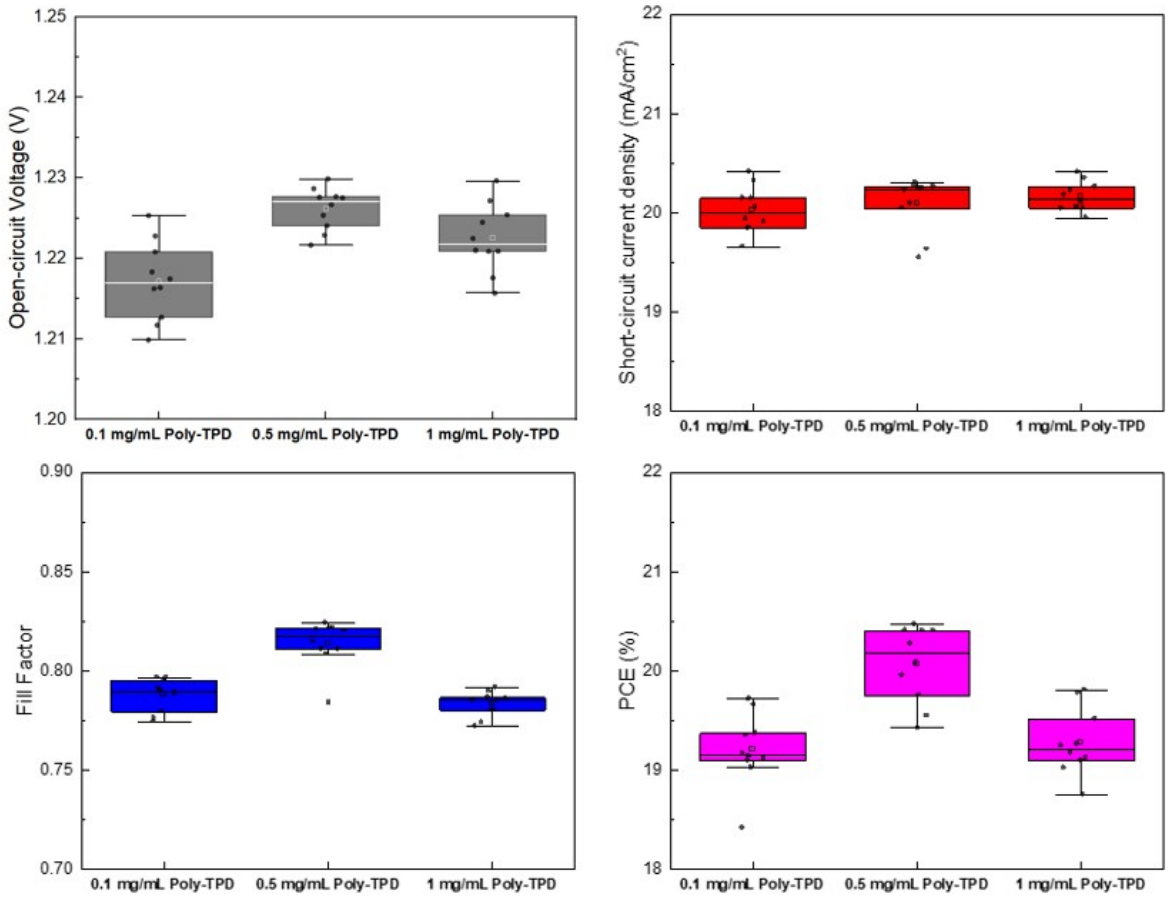

Fig S7. Statistical photovoltaic parameters of ten individual devices from three separate batches including V_{oc}, J_{sc}, FF and PCE of single-junction perovskite solar cells with Poly-TPD/Spiro-TTB bilayer HTL, by varying the Poly-TPD precursor concentrations.

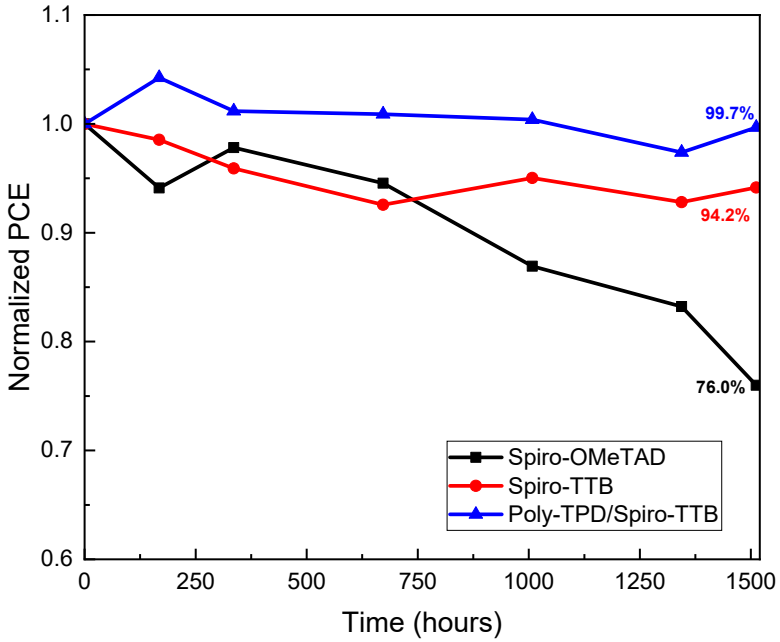

Fig S8. Efficiency evolution of encapsulated single-junction PSCs with edge sealing based on different HTLs including Spiro-OMeTAD, Spiro-TTB and Poly-TPD/Spiro-TTB bilayer stored in ambient at 25 °C / 40~60% RH.

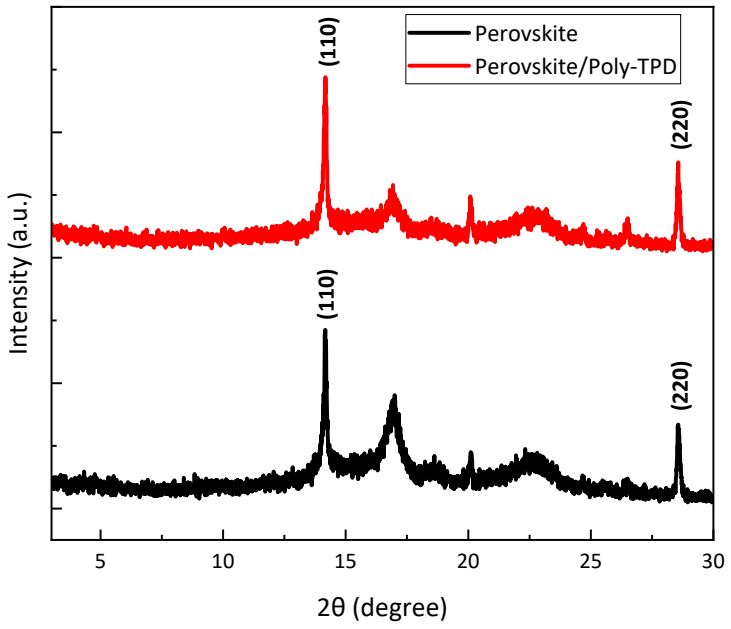

Fig S9. XRD patterns of pristine perovskite film and the one with poly-TPD layer coating, respectively.

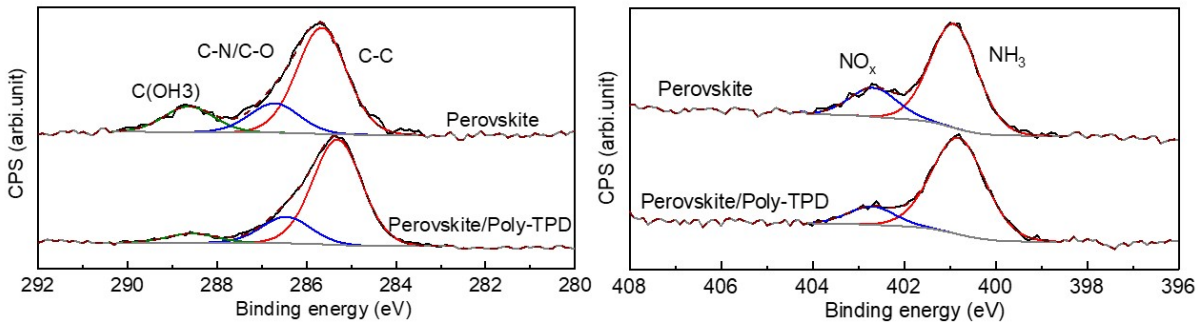

Fig S10. The X-ray photoelectron spectroscopy (XPS) curves analysing the binding energy of carbon (left) and nitrogen bonds (right) including of pristine perovskite film and perovskite film with poly-TPD layer, respectively.

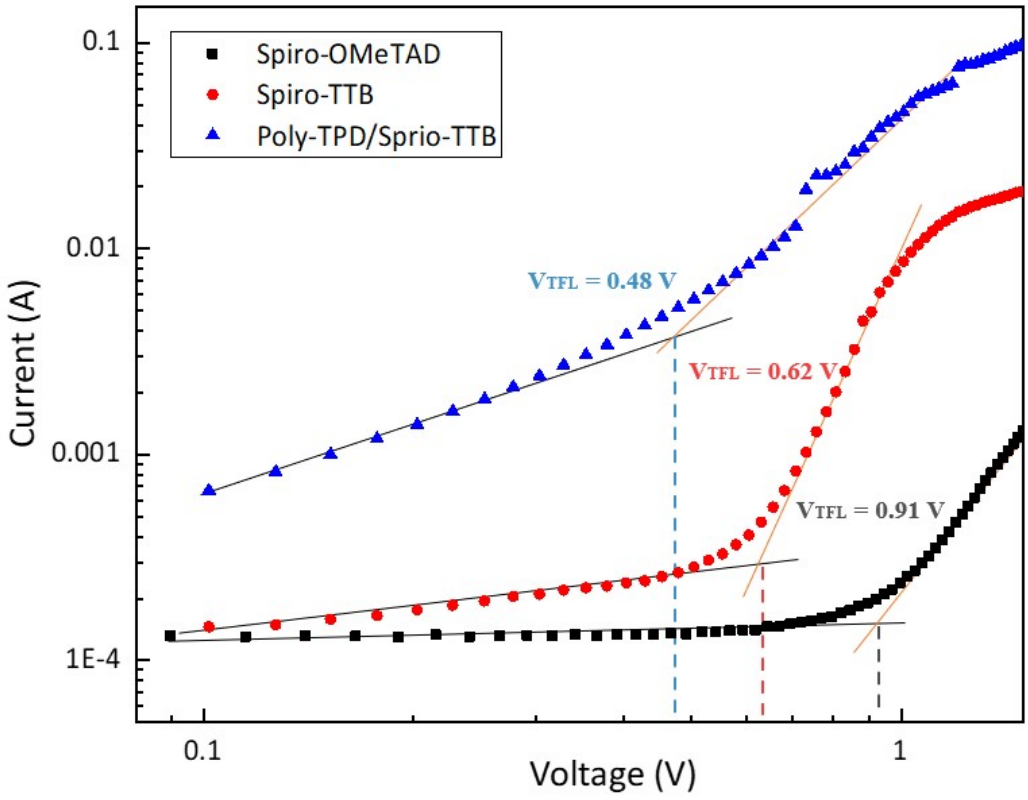

Fig S11. The space charge limited current (SCLC) curves and the calculated trap-filled limited voltage (V_{TFL}) of device with the structure of glass/FTO/PTAA/perovskite/HTLs/Au based on different HTLs including Spiro-OMeTAD, Spiro-TTB and Poly-TPD/Spiro-TTB bilayer.

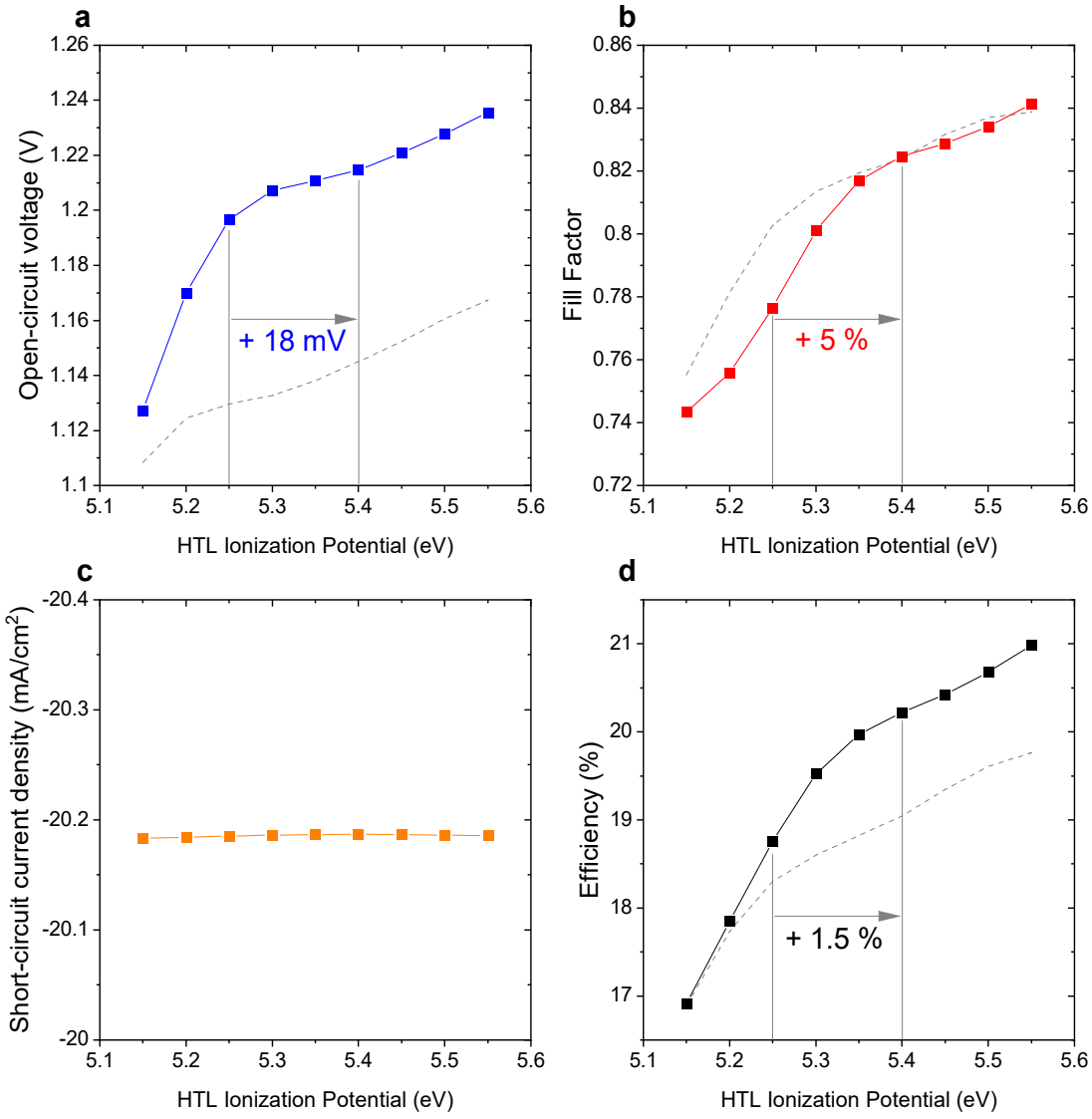

Fig S12. Simulated dependence of (a) *V*oc, (b) FF, (c) *J*sc and (d) PCE as a function of HTL ionization potential. The solid lines represent results for a cell with a 1.68eV-bandgap perovskite. The dashed lines show the same simulations for a cell with 1.60 eV bandgap. The arrows indicate the change from HTL IP = 5.25 to 5.4 eV, consistent with the change in IP for the experimental shift between Poly-TPD and Spiro-TTB. The larger bandgap cell benefits disproportionately from a larger HTL ionization potential, relative to a 1.60 eV bandgap perovskite.

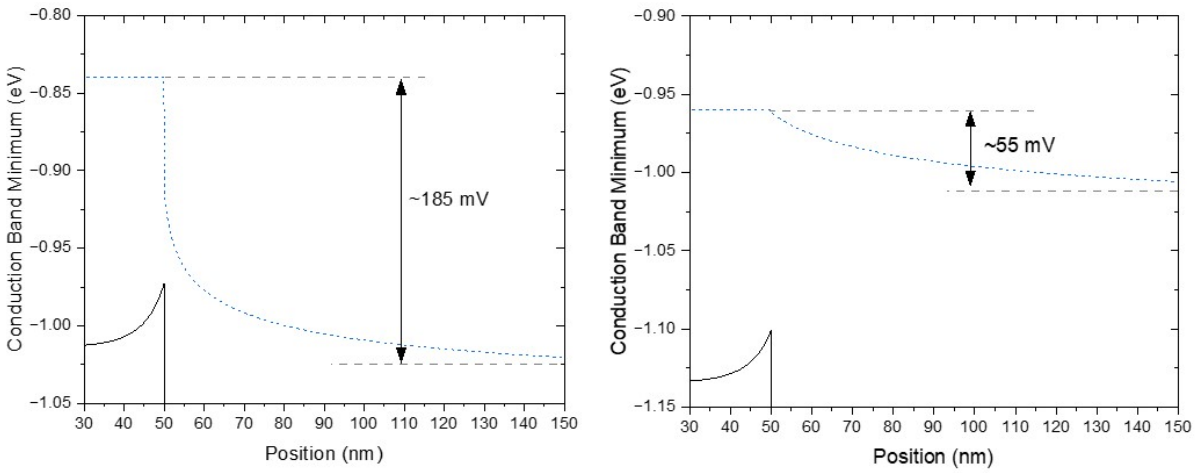

Fig S13. Energy band diagram of perovskite solar cell at perovskite-HTL interface, for IP_{HTL} = 2.25 eV, and without any non-radiative recombination. Hole depletion contributes ~25 mV of transport losses, but this is substantially less than in the case with non-radiative recombination as shown in **Fig S13**.

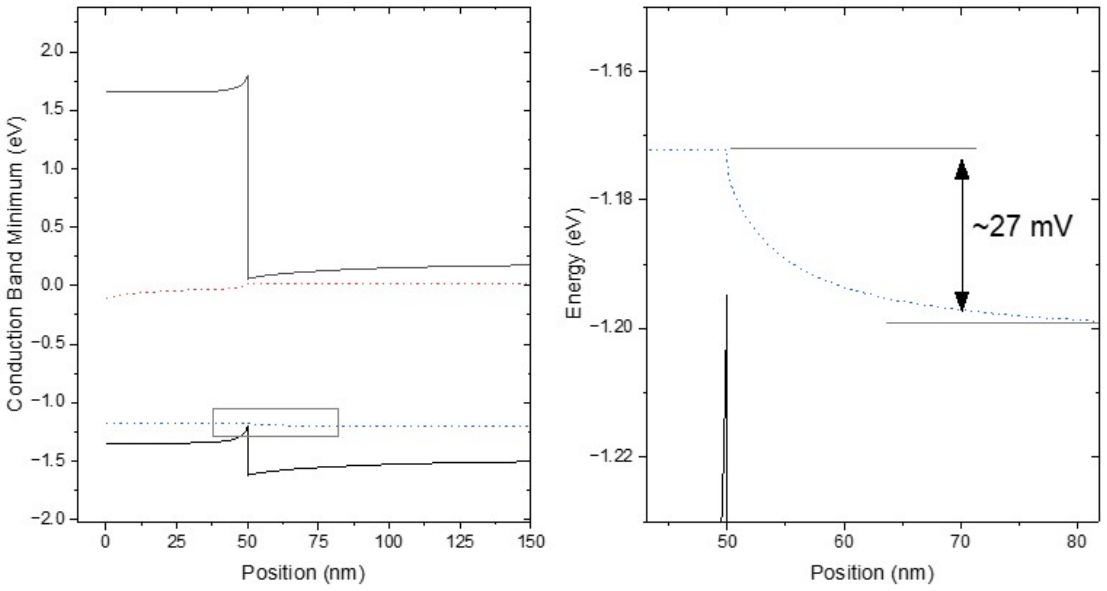

Fig S14. Energy diagram of quasi-Fermi level for holes at perovskite-HTL interface for (left) IP_{HTL} = 2.25 eV, and (right) IP_{HTL} = 2.40 eV at 20 mA/cm^2. In the latter case, hole transport losses are 130 mV lower than in the former case.

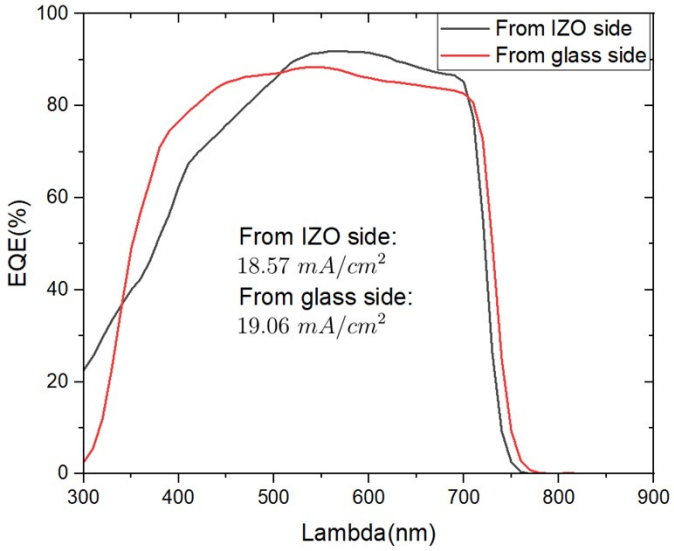

Fig. S15. EQE of the semitransparent perovskite solar cell based Poly-TPD/Spiro-TTB bilayer as the HTL.

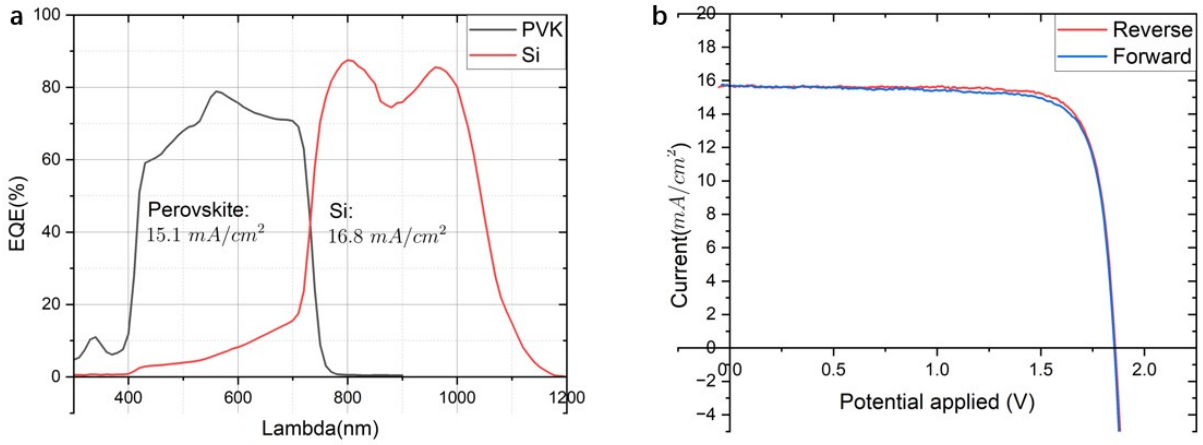

Fig. S16, a) EQE and b) *J-V* curve of the perovskite/Si tandem solar cells based on Spiro-OMeTAD as the HTL.

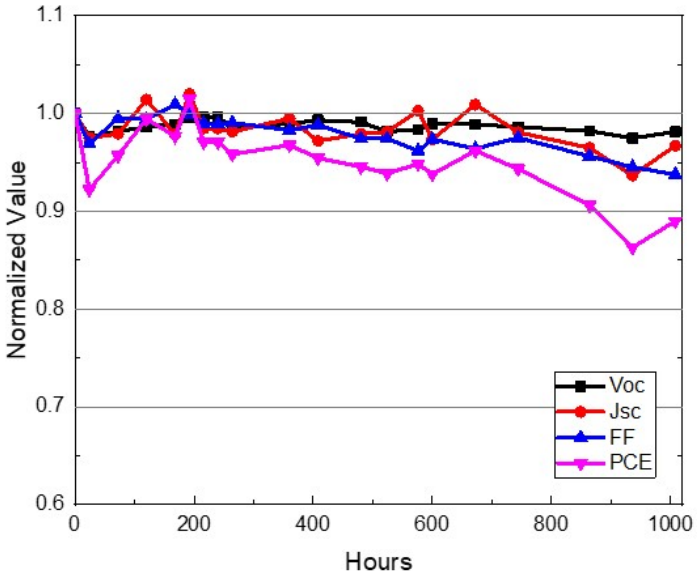

Fig S17. Damp-heat stability test of encapsulated monolithic perovskite/Si tandem solar cells indicated by the normalized V_{oc}, J_{sc}, FF and PCE versus time, with the device stored in the environmental chamber with 85 °C /85% relative humidity (RH) in dark.

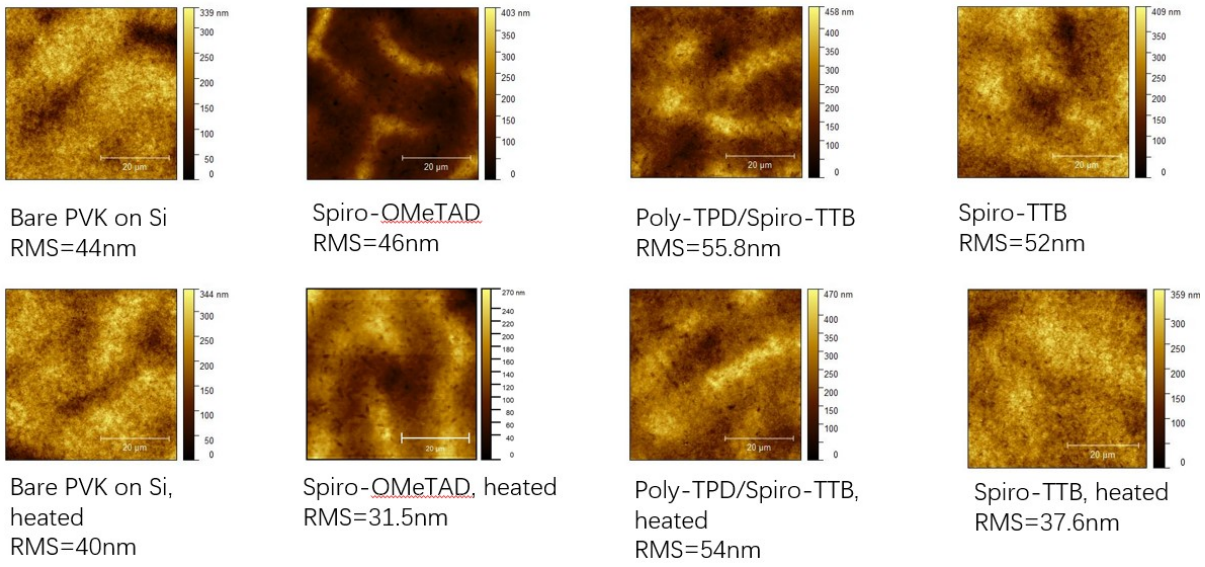

Fig S18. AFM images of the pristine perovskite film and different HTLs of Spiro-OMeTAD, Spiro-TTB, and Poly-TPD/Spiro-TTB bilayer on perovskite film before (the top line) and after the thermal aging at 85 °C for 30 min (the bottom line). While the morphology of the Spiro-OMeTAD film undergoes drastic changes, that of the Spiro-TTB and Poly-TPD/Spiro-TTB undergoes only minor alterations, indicating the excellent thermal stability of the latter. This observation aligns with the *I-V* curves shown in Fig. S2.

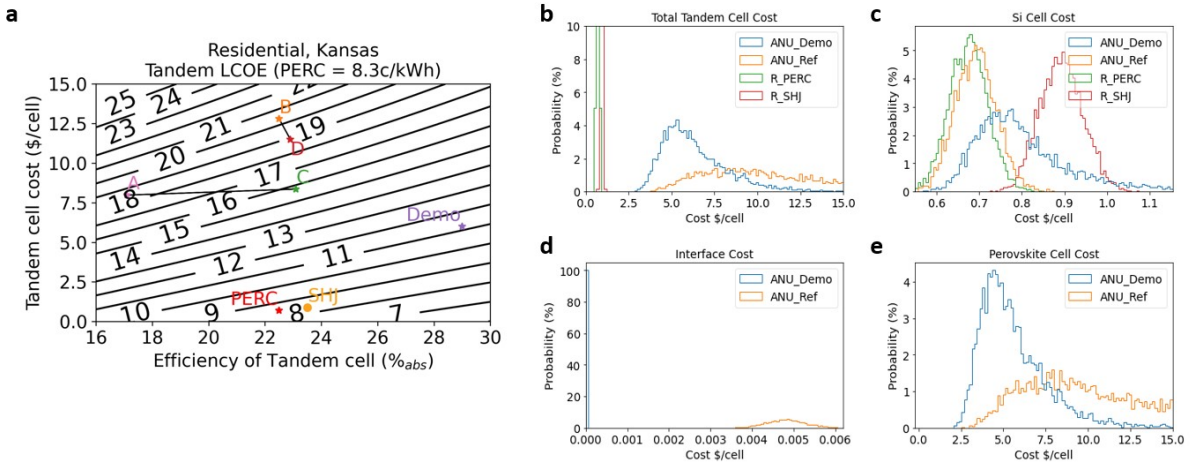

Fig S19. **a**, LCOE estimate taken from previous work,[7] which shows four *n-i-p* tandem cells (A, B, C and D defined in the referenced paper, D is ANU_Ref in this paper), with the new demonstrated tandem at lower cost and higher efficiency (labelled 'Demo). Histograms of the cost of ANU_Ref and ANU_Demo compared to reference PERC and SHJ c-Si cells. **b**, shows the total cost, **c**, the Si cell processes, **d**, the interface between the Si and perovskite cells, and **e**, the perovskite cell processes.

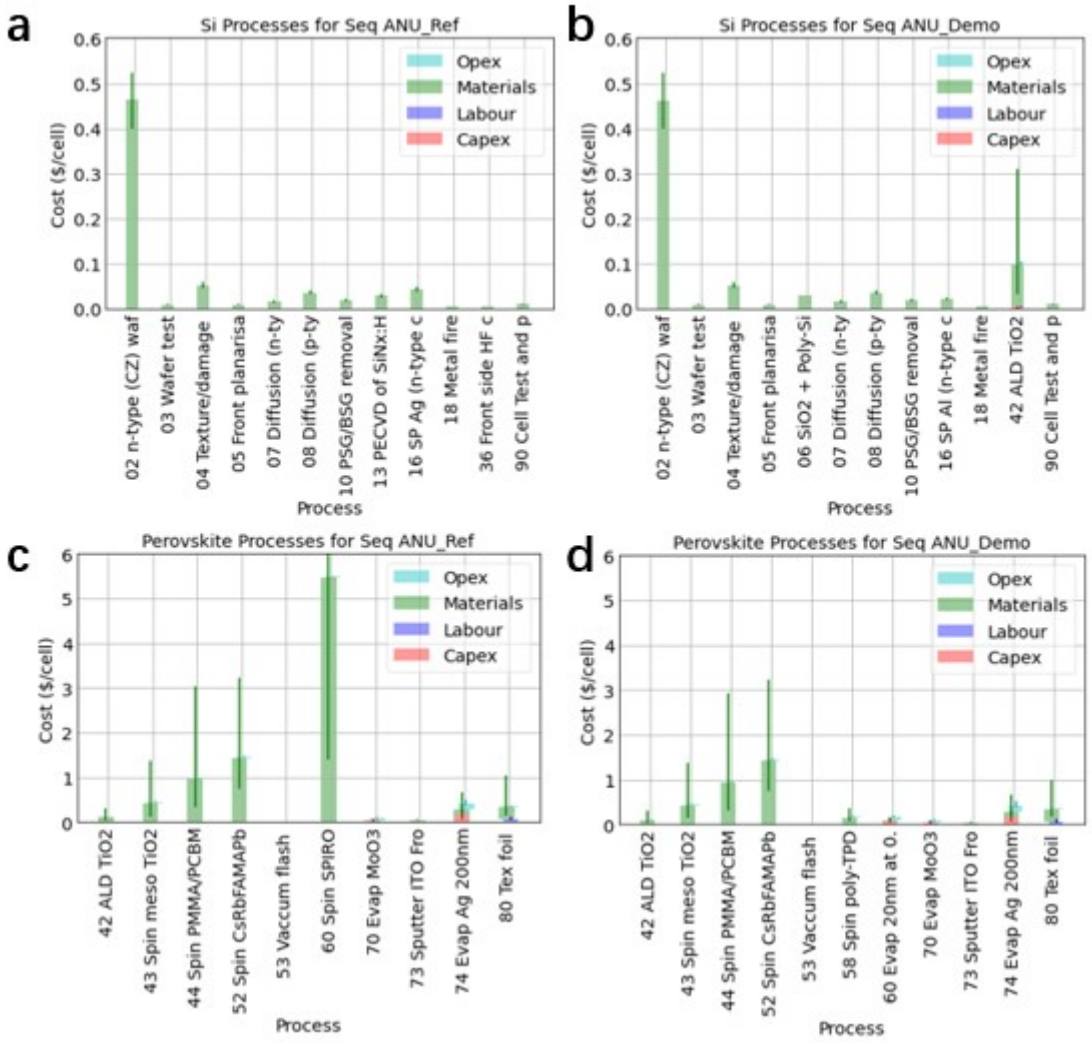

Fig S20. Process step costs for ANU_Ref (left) and ANU_Demo (right), for the Si processes (top) and perovskite processes (bottom). Error bars indicate the 10^{th} and 90^{th} percentile values of the cost of that cost component in the Monte Carlo model. Following the convention of Chang's work, the c-Si processing costs are taken from literature and are shown as a "material cost", and not divided into capex, labour, materials and opex. For presenting a conservative estimate of the cost, we opted to use a relatively thick TiO_2 layer in our cost study. In practice, a thinner TiO_2 layer, equivalent to half of the thickness employed in the technoeconomic study (54 nm), has proven to be effective in the current tandem design. Therefore, the overall cost of the ALD TiO_2 discussed here falls at the upper end of the estimation.

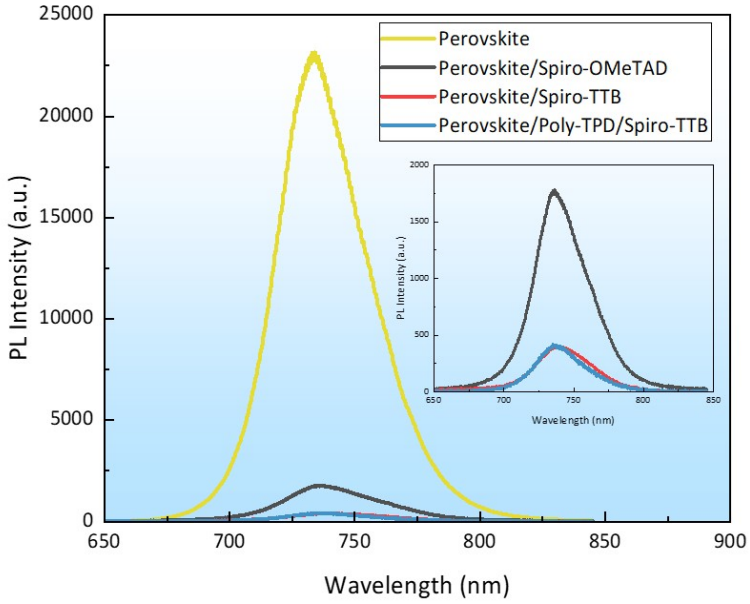

Fig S21. Steady-state PL spectral of samples with the structure of glass/FTO/perovskite/HTLs based on different HTLs including Spiro-OMeTAD, Spiro-TTB and Poly-TPD/Spiro-TTB bilayer. The inset shows the comparison of the PL spectra of the samples with HTLs.

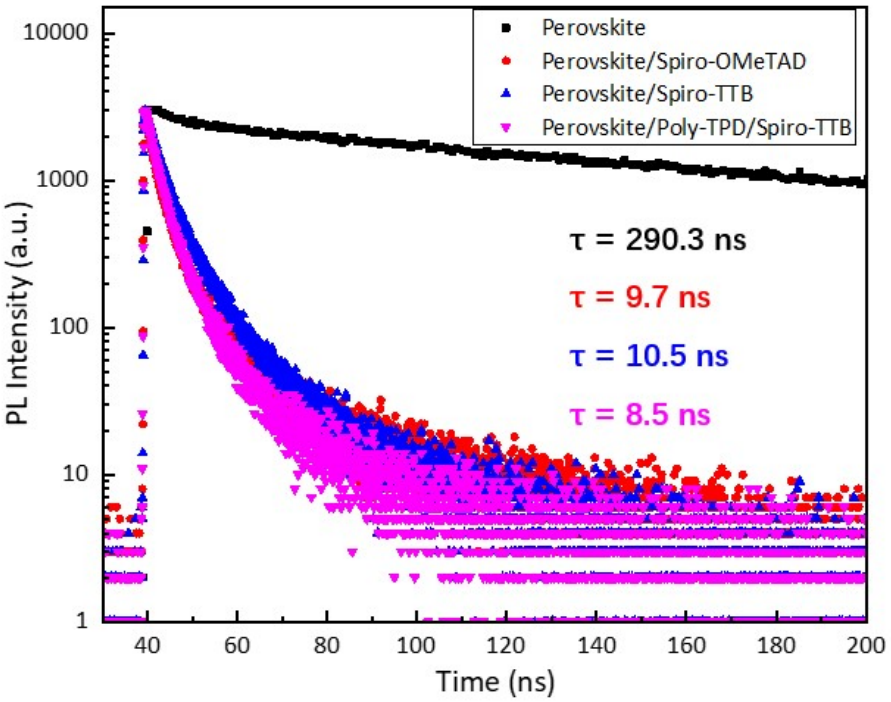

Fig S22. Time-resolved PL spectral of samples with the structure of glass/FTO/perovskite/HTLs based on different HTLs including Spiro-OMeTAD, Spiro-TTB and Poly-TPD/Spiro-TTB bilayer.

To investigate the charge carrier dynamics, steady-state and time-resolved PL measurements were carried out on pristine perovskite films as well as perovskite films with various HTLs. The PL peaks

for all samples were found to be around 730 nm, with the perovskite films incorporating HTLs exhibiting strong PL quenching **(Fig. S24)**, indicating effective transfer of charge carriers across the perovskite/charge transport layer (CTL) interface.[13, 14] Stronger PL quenching in Spiro-TTB and Poly-TPD/Spiro-TTB based perovskite films indicates that the light-excited electron-hole pairs in the perovskite film are quickly separated at both perovskite/HTL interfaces, revealing their higher charge transfer efficiency, the latter of which exhibits slightly stronger quenching than the Spiro-TTB based film at the wavelength range from 750 to 800 nm, indicating superior charge transfer ability of the bilayer HTL. The lifetime of the charged carriers in perovskite film with different HTLs decreased dramatically as shown in **Fig. S25** respectively.

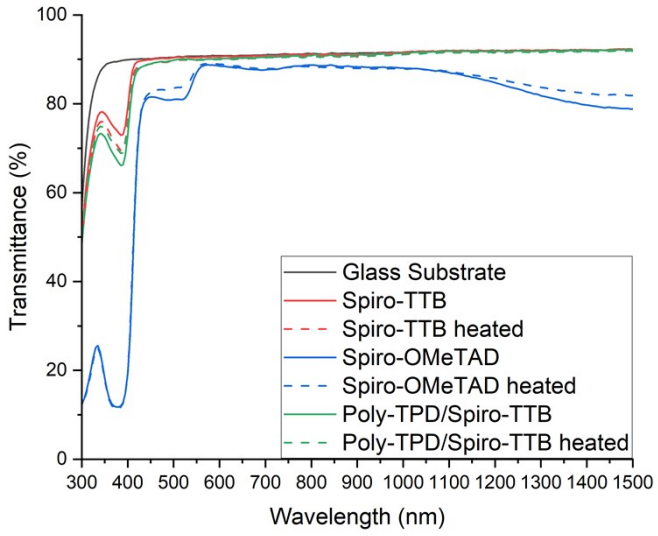

Fig S23. Transmittance of different HTLs of Spiro-OMeTAD, Spiro-TTB, and Poly-TPD/Spiro-TTB bilayer before and after the thermal aging at 85 °C for 30 min. The test structure is based on Glass/HTLs.

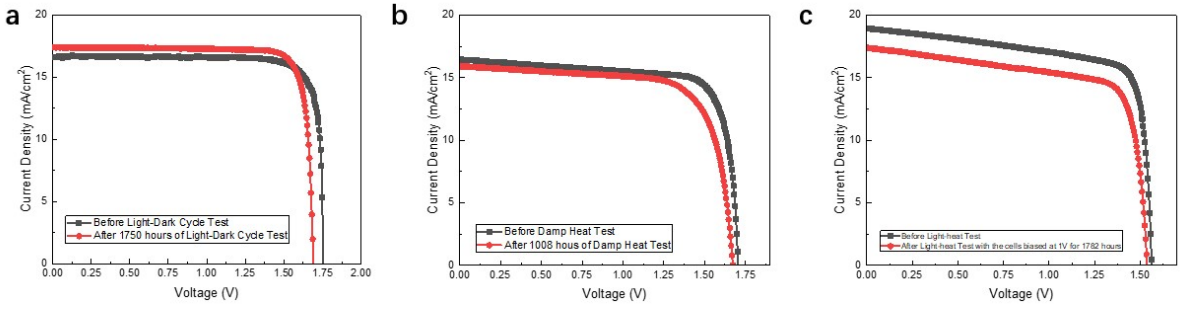

Fig S24. The *J-V* curve of the encapsulated perovskite/Si tandem solar cell before and after a) undergoing over 1750 hours of light-dark cycle test under open-circuit condition (72 light-dark cycles with each cycle containing 12 hours of light illumination and 12 hours in dark) b) damp-heat test by aging in the environmental chamber with 85 °C / 85% RH in dark and c) biased at 1V and under continuous 1-sun illumination at 55 ± 5°C in ambient for 1000 hours.

We note that there is performance discrepancy, particularly in current density, between the bare tandem cells and the encapsulated ones. This is primarily caused by the loss incurred during the encapsulation process. This can be mitigated through optimisation of the encapsulation structure and process to reduce the optical losses due to additional glasses, reduce electrical losses by connecting the evaporated metal electrode with external wires, and minimize the potential damage caused by exposing the cells to soldering in the ambient.

References

1. D. Yan, A. Cuevas, Y. Wan and J. Bullock, *Solar Energy Materials and Solar Cells*, 2016, **152**, 73-79.
2. D. Yan, A. Cuevas, J. Bullock, Y. Wan and C. Samundsett, *Solar Energy Materials and Solar Cells*, 2015, **142**, 75-82.
3. H. Shen, T. Omelchenko Stefan, A. Jacobs Daniel, S. Yalamanchili, Y. Wan, D. Yan, P. Phang, T. Duong, Y. Wu, Y. Yin, C. Samundsett, J. Peng, N. Wu, P. White Thomas, G. Andersson Gunther, S. Lewis Nathan and R. Catchpole Kylie, *Science Advances*, 2018, **4**, eaau9711.
4. J. Liu, E. Aydin, J. Yin, M. De Bastiani, F. H. Isikgor, A. U. Rehman, E. Yengel, E. Ugur, G. T. Harrison, M. Wang, Y. Gao, J. I. Khan, M. Babics, T. G. Allen, A. S. Subbiah, K. Zhu, X. Zheng, W. Yan, F. Xu, M. F. Salvador, O. M. Bakr, T. D. Anthopoulos, M. Lanza, O. F. Mohammed, F. Laquai and S. De Wolf, *Joule*, 2021, **5**, 3169-3186.
5. J. Peng, F. Kremer, D. Walter, Y. Wu, Y. Ji, J. Xiang, W. Liu, T. Duong, H. Shen, T. Lu, F. Brink, D. Zhong, L. Li, O. Lee Cheong Lem, Y. Liu, K. J. Weber, T. P. White and K. R. Catchpole, *Nature*, 2022, **601**, 573-578.
6. J. Peng, D. Walter, Y. Ren, M. Tebyetekerwa, Y. Wu, T. Duong, Q. Lin, J. Li, T. Lu, M. A. Mahmud, O. L. C. Lem, S. Zhao, W. Liu, Y. Liu, H. Shen, L. Li, F. Kremer, H. T. Nguyen, D.-Y. Choi, K. J. Weber, K. R. Catchpole and T. P. White, *Science*, 2021, **371**, 390-395.
7. N. L. Chang, J. Zheng, Y. Wu, H. Shen, F. Qi, K. Catchpole, A. Ho-Baillie and R. J. Egan, *Progress in Photovoltaics: Research and Applications*, 2021, **29**, 401-413.
8. B. Kafle, B. S. Goraya, S. Mack, F. Feldmann, S. Nold and J. Rentsch, *Solar Energy Materials and Solar Cells*, 2021, **227**, 111100.
9. N. L. Chang, G. K. Poduval, B. Sang, K. Khoo, M. Woodhouse, F. Qi, M. Dehghanimadvar, W. M. Li, R. J. Egan and B. Hoex, *Progress in Photovoltaics: Research and Applications*, 2023, **31**, 414-428.
10. H. H. Pham and L.-W. Wang, *Physical Chemistry Chemical Physics*, 2015, **17**, 541-550.
11. M. T. McDowell, M. F. Lichterman, A. I. Carim, R. Liu, S. Hu, B. S. Brunschwig and N. S. Lewis, *ACS Applied Materials & Interfaces*, 2015, **7**, 15189-15199.
12. V. Sittinger, P. S. C. Schulze, C. Messmer, A. Pflug and J. C. Goldschmidt, *Opt. Express*, 2022, **30**, 37957-37970.
13. D. Stranks Samuel, E. Eperon Giles, G. Grancini, C. Menelaou, J. P. Alcocer Marcelo, T. Leijtens, M. Herz Laura, A. Petrozza and J. Snaith Henry, *Science*, 2013, **342**, 341-344.
14. T. Kirchartz, J. A. Márquez, M. Stolterfoht and T. Unold, *Advanced Energy Materials*, 2020, **10**, 1904134.